Electronic supplementary information (ESI) for

Highly conductive and stable Co_9S_8 thin films by atomic layer deposition: from process development and film characterization to selective and epitaxial growth

Miika Mattinen, [‡a] Timo Hatanpää, [a] Kenichiro Mizohata, [b] Jyrki Räisänen, [b] Markku Leskelä, [a] and Mikko Ritala *[a]

[a] Department of Chemistry, University of Helsinki, P.O. Box 55, FI-00014, Finland

[b] Department of Physics, University of Helsinki, P.O. Box 43, FI-00014, Finland

‡ Present address: Department of Applied Physics, Eindhoven University of Technology, P.O. Box 513, 5600 MB Eindhoven, The Netherlands

*email: mikko.ritala@helsinki.fi

Contents

S1. Thermodynamic calculations of formation of CoS_x phases

Thermodynamic calculations show that formation of cobalt sulfide of different stoichiometries (Co_9S_8, CoS, Co_3S_4, and CoS_2) is favorable from $CoCl_2$ and H_2S in the temperature range of the ALD experiments performed (Fig. S1). It can be seen that the Gibbs free energies for different CoS_x phases, approximately -125 to -145 kJ/mol of $CoCl_2$ at 180–300 °C are very similar, less than 15 kJ/mol apart. Therefore, it is not surprising that the calculations cannot correctly predict which CoS_x phase is formed. Actually, Co_9S_8 is the least favorable (i.e. least negative ΔG) of the phases according to the calculations. This may be due to limitations of our calculations, including that they do not specifically account for surface reactions, the used thermodynamic data has unknown uncertainties, the byproducts for the reactions requiring reduction/oxidation are unconfirmed even if they are chemically plausible (different S_x vapor phase species ($2 \leq x \leq 8$) were evaluated and found to have a negligible effect on the calculated ΔG, S_8 being the most stable under the conditions evaluated), and kinetic effects are not included. The reactions used in the calculations (balanced for $CoCl_2$ for comparability) were:

Co_9S_8: $CoCl_2\,(g) + H_2S\,(g) \rightarrow 1/9Co_9S_8 + 2HCl\,(g) + 1/72S_8\,(g)$

CoS: $CoCl_2\,(g) + H_2S\,(g) \rightarrow CoS + 2HCl\,(g)$

Co_3S_4: $CoCl_2\,(g) + 4/3H_2S\,(g) \rightarrow 1/3Co_3S_4 + 2HCl\,(g) + 1/3H_2\,(g)$

CoS_2: $CoCl_2\,(g) + 2H_2S\,(g) \rightarrow CoS_2 + 2HCl\,(g) + H_2\,(g)$

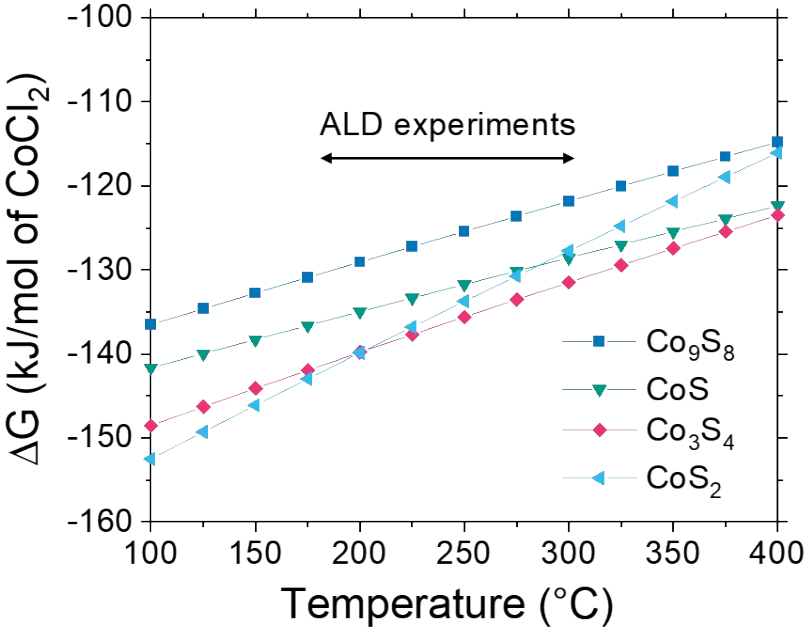

Fig. S1 Thermodynamic calculations of ΔG for the formation of different CoS_x phases from $CoCl_2$ and H_2S using Outokumpu HSC Chemistry for Windows (version 5.11).

S2. Additional results of deposition experiments

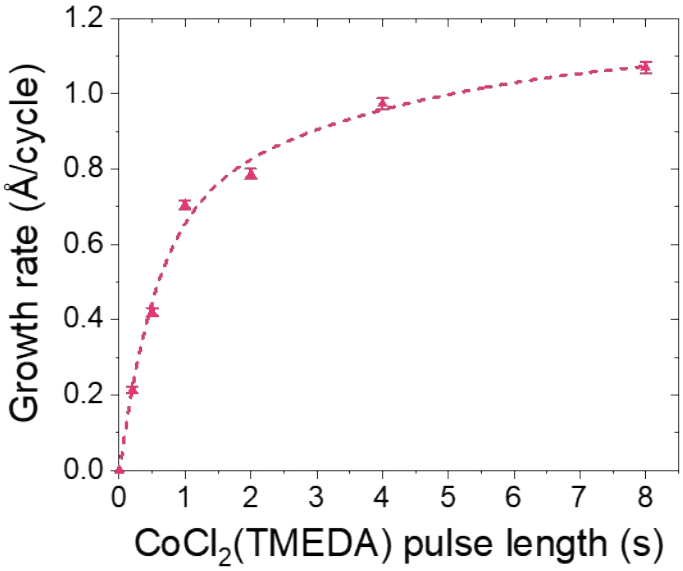

Fig. S2 Growth rate as a function of $CoCl_2$(TMEDA) pulse at 275 °C, showing also a 8.0 s pulse. The films were deposited on silicon (native oxide) using 1000 cycles with varied $CoCl_2$(TMEDA) and 2.0 s H_2S pulses separated by 1.0 s N_2 purges. The thicknesses were measured by EDS. The error bars represent statistical measurement uncertainty (one standard deviation). The line represents an exponential fit meant to guide the eye.

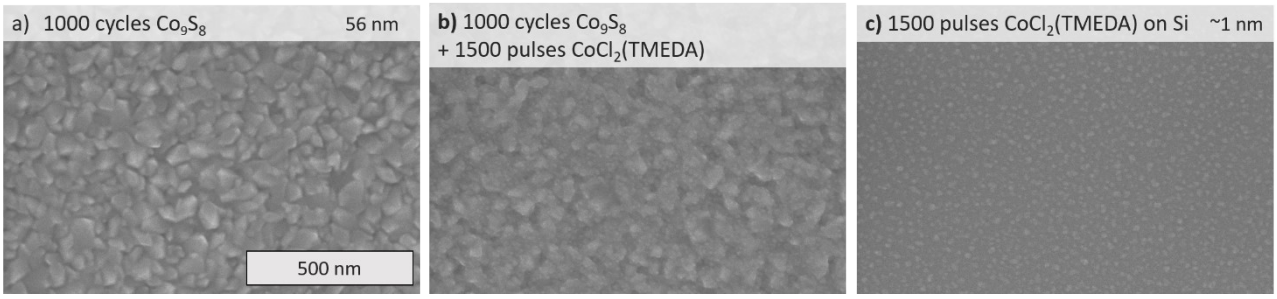

Fig. S3 SEM images and EDS thicknesses of a) an as-deposited Co_9S_8 film (1000 cycles, 1.0 s $CoCl_2$(TMEDA) and 2.0 s H_2S pulses with 1.0 s purges), b) the Co_9S_8 film after 1500 additional four-second $CoCl_2$(TMEDA) pulses that shows negligible increase in thickness and a slight change in morphology, and c) silicon (native oxide) substrate after 1500 four-second $CoCl_2$(TMEDA) pulses showing negligible film growth due to precursor decomposition. All pulses were applied at 275 °C.

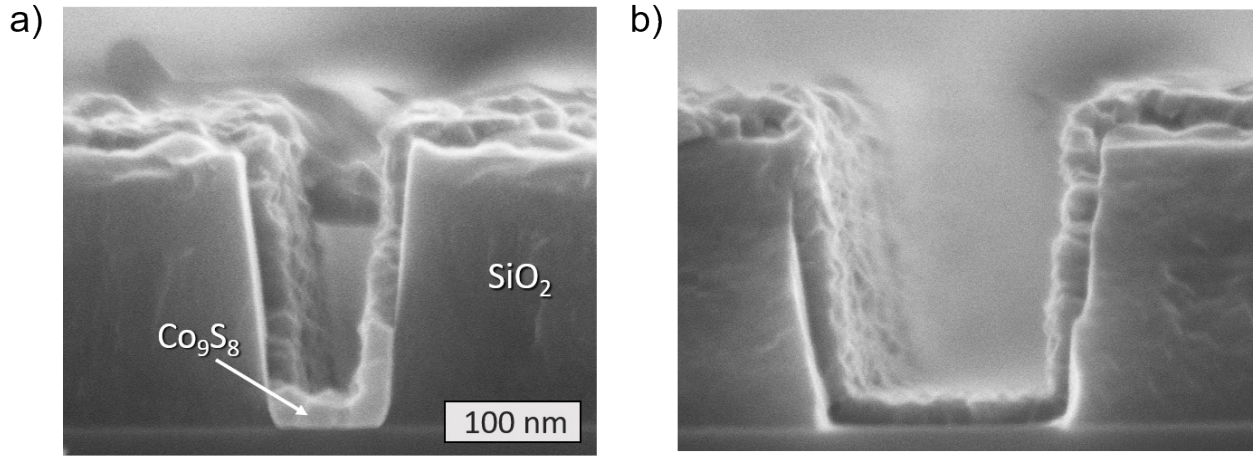

Fig. S4 SEM images demonstrating conformal coverage of Co_9S_8 on trench structures with aspect ratios of approximately a) two and b) one. Note that the trenches are slightly tilted from left to right in the image and the film was removed from some parts of the cross section when the sample was prepared by cleaving. The film was deposited at 275 °C using 500 cycles with 2.0 s $CoCl_2$(TMEDA) and H_2S pulses separated by 5.0 s purges.

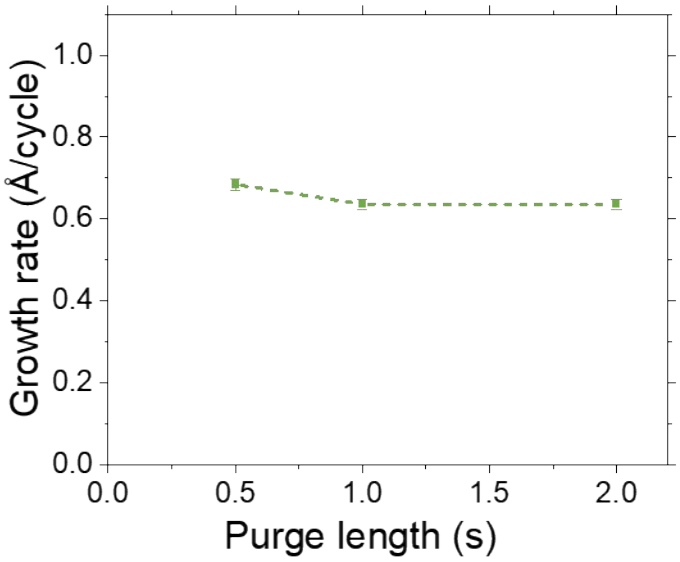

Fig. S5 Growth rate as a function of purge lengths (both purge steps varied simultaneously). The films were deposited on silicon (native oxide) at 275 °C using 1000 cycles with 1.0 s $CoCl_2$(TMEDA) and 2.0 s H_2S pulses. The thicknesses were measured by EDS. The error bars represent statistical measurement uncertainty (one standard deviation).

S3. Effect of pulse times on morphology, texture, and growth rate

The effect of the pulse lengths on crystallinity and morphology at 275 °C was studied to understand the atypical saturation characteristics. When the $CoCl_2$(TMEDA) pulse length was increased from 0.2 s to 8.0 s, the size of the grains visible on the surface decreased somewhat despite a four-fold increase in film thickness (Fig. S6). The grain shape also changed, becoming more pyramidal with long pulses. At the same time, the preferred orientation changed from (111) at short pulses toward (113) at long $CoCl_2$(TMEDA) pulses, which coincided with an increase in growth rate (Fig. S2,S7). Increasing the length of the H_2S pulse had a smaller but opposite effect on morphology, crystallinity and growth rate. Namely, an increase in the (111) texture and decrease in growth rate was seen upon elongation of the H_2S pulse (Fig. S8,S9). In contrast, the changes in texture when varying only the film thickness were small (Fig. S16).

The pulse length dependence of texture and growth rate at 275 °C may be explained by different crystalline facets having different growth rates due to different densities of reactive groups on them. The dependence of ALD growth rate on the density of reactive groups is a well-known phenomenon and in line with the surface-limited nature of ALD.[1] Indeed, the development of preferred orientation (texture) in ALD films may be considered a result of orientation dependent growth rate.[2] While the orientation dependency of growth rate applies to most if not all crystalline ALD films, the abnormally slow saturation observed at 275 °C is rather unique to this process and temperature and requires further explanation. One possibility is slowness of growth kinetics (i.e. Å/s) on the facets with the highest growth rates (Å/cycle). In this case, the facets with a low growth rate but fast kinetics would dominate at short pulse lengths, while the facets with a higher growth rate but slower kinetics would lead to a slower increase of the growth rate at longer pulse lengths. As reaction rates rapidly increase with increasing temperature, this would also explain why the slow saturation is observed only at 275 °C: the slow reactions potentially leading to a higher growth rate are too slow to be observed at all at lower temperatures. This is also in line with the growth rate increasing toward higher

temperatures and reaching its maximum at 275 °C. Finally, we note that unlike alternate explanations based on long pulses simply giving more time for slow surface reaction or diffusion processes and thus resulting in a higher GPC when the cycle length is elongated, our suggestion can explain the opposite trends observed for $CoCl_2$(TMEDA) and H_2S.

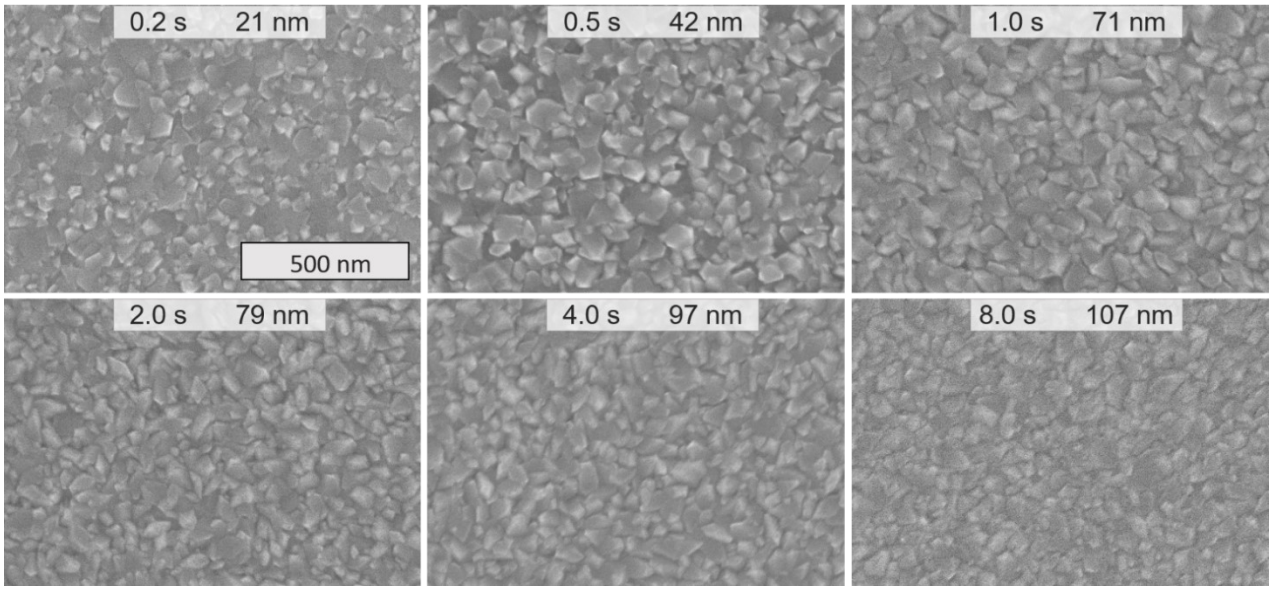

Fig. S6 SEM images of films deposited using different $CoCl_2$(TMEDA) pulse lengths. The films were grown on silicon (native oxide) at 275 °C using 1000 cycles with 2.0 s H_2S pulses and 1.0 s purges. Thicknesses determined by EDS are indicated.

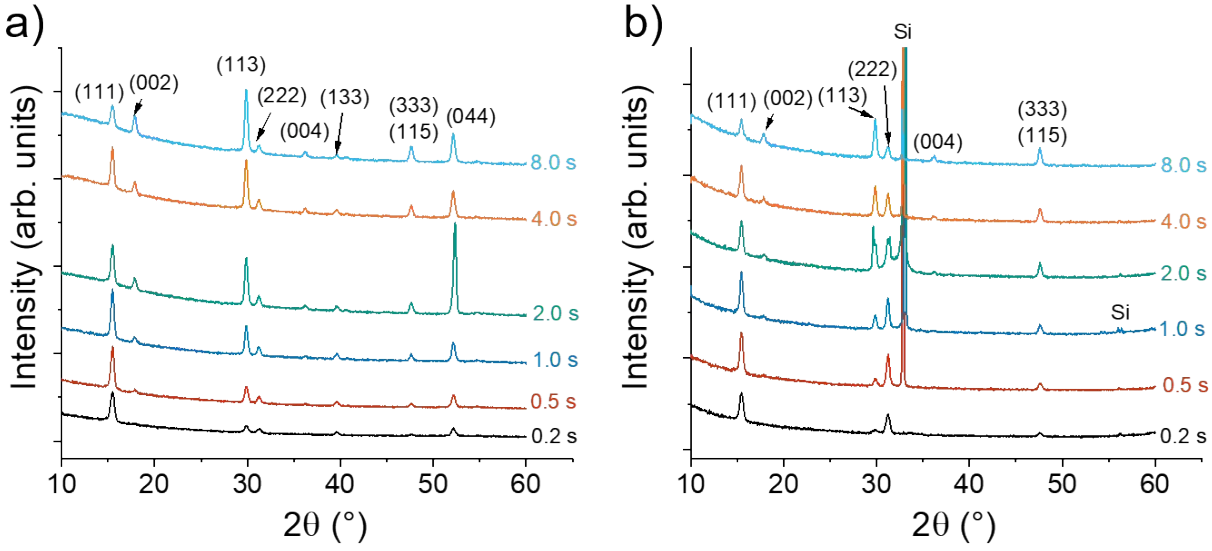

Fig. S7 (a) Grazing incidence and (b) θ-2θ X-ray diffractograms of films deposited using different $CoCl_2$(TMEDA) pulse lengths. The films were grown on silicon (native oxide) at 275 °C using 1000 cycles with 2.0 s H_2S pulses and 1.0 s purges. All peaks were attributed to either Co_9S_8 (Miller indices marked) or Si substrate.

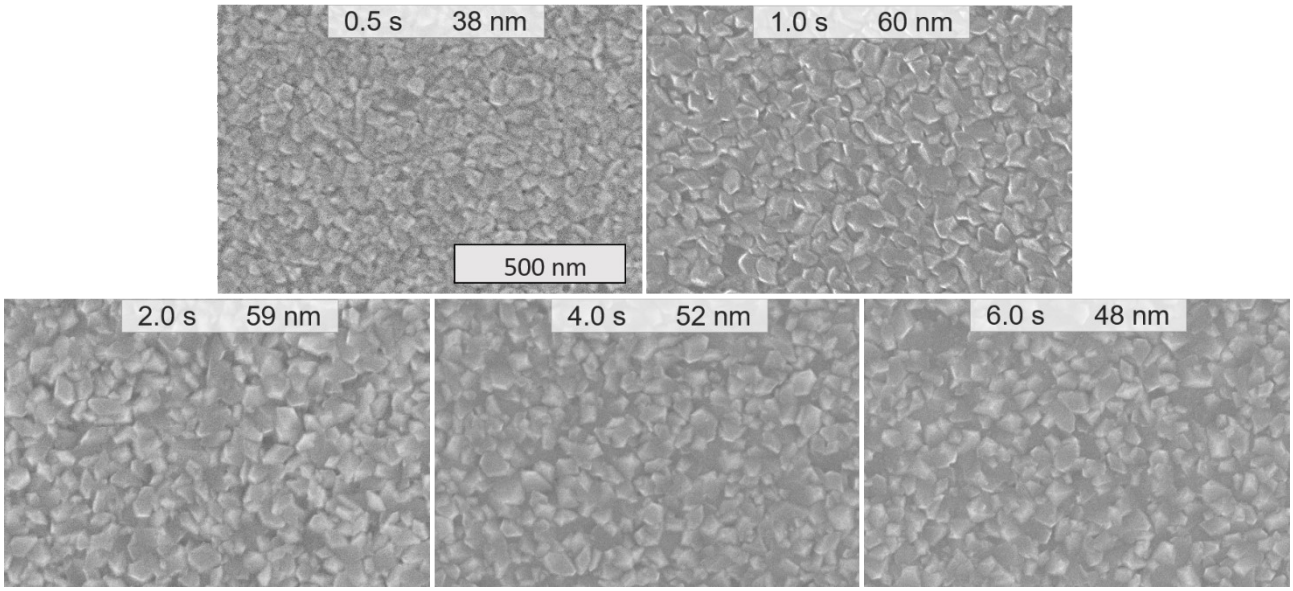

Fig. S8 SEM images of films deposited using different H_2S pulse lengths. The films were grown on silicon (native oxide) at 275 °C using 1000 cycles with 1.0 s $CoCl_2$(TMEDA) pulses and 1.0 s purges. Thicknesses determined by EDS are indicated.

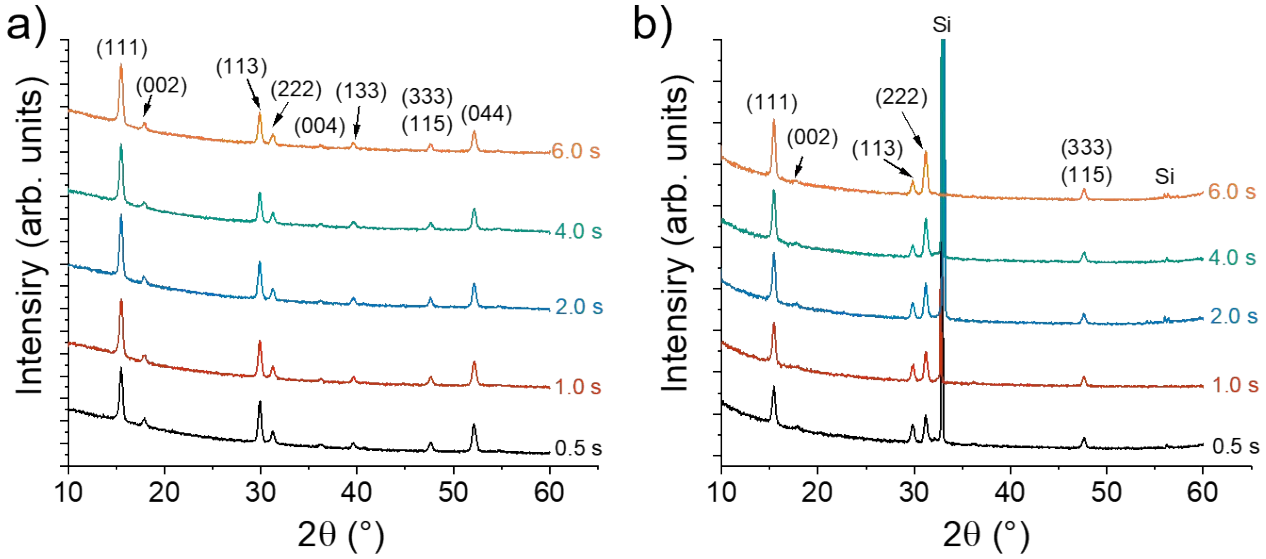

Fig. S9 (a) Grazing incidence and (b) θ-2θ X-ray diffractograms of films deposited using different H_2S pulse lengths. The films were grown on silicon (native oxide) at 275 °C using 1000 cycles with 1.0 s $CoCl_2$(TMEDA) pulses and 1.0 s purges. All peaks were attributed to either Co_9S_8 (Miller indices marked) or Si substrate.

S4. Effect of deposition temperature

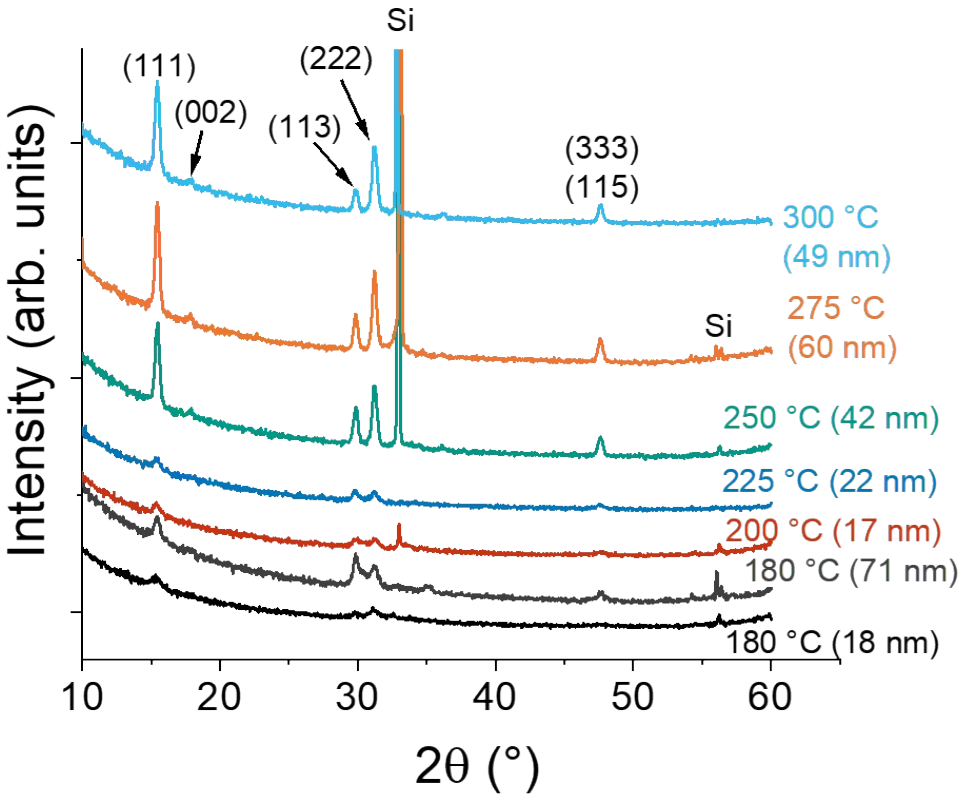

Fig. S10 θ-2θ X-ray diffractograms of films deposited at different temperatures. The films were deposited on silicon (native oxide) using 1000 cycles except for the thicker film at 180 °C deposited using 3000 cycles. Thicknesses determined by EDS are indicated. All peaks were attributed to either Co_9S_8 (Miller indices marked) or the Si substrate. The relative intensities of different reflections in a randomly oriented sample are 35 $^{(111)}$: 6 $^{(002)}$: 88 $^{(113)}$: 27 $^{(222)}$: 100 $^{(044)}$ according to data from Crystallography Open Database (COD), no. 1011206. Notably, the $^{(044)}$ reflection at 52.0 °2θ that has the highest intensity in randomly oriented Co_9S_8 was missing from all of the measured films. The $^{(333)}$ and $^{(115)}$ reflections overlap, and therefore cannot be used for determining preferred orientation.

S5. Compositional depth profiles

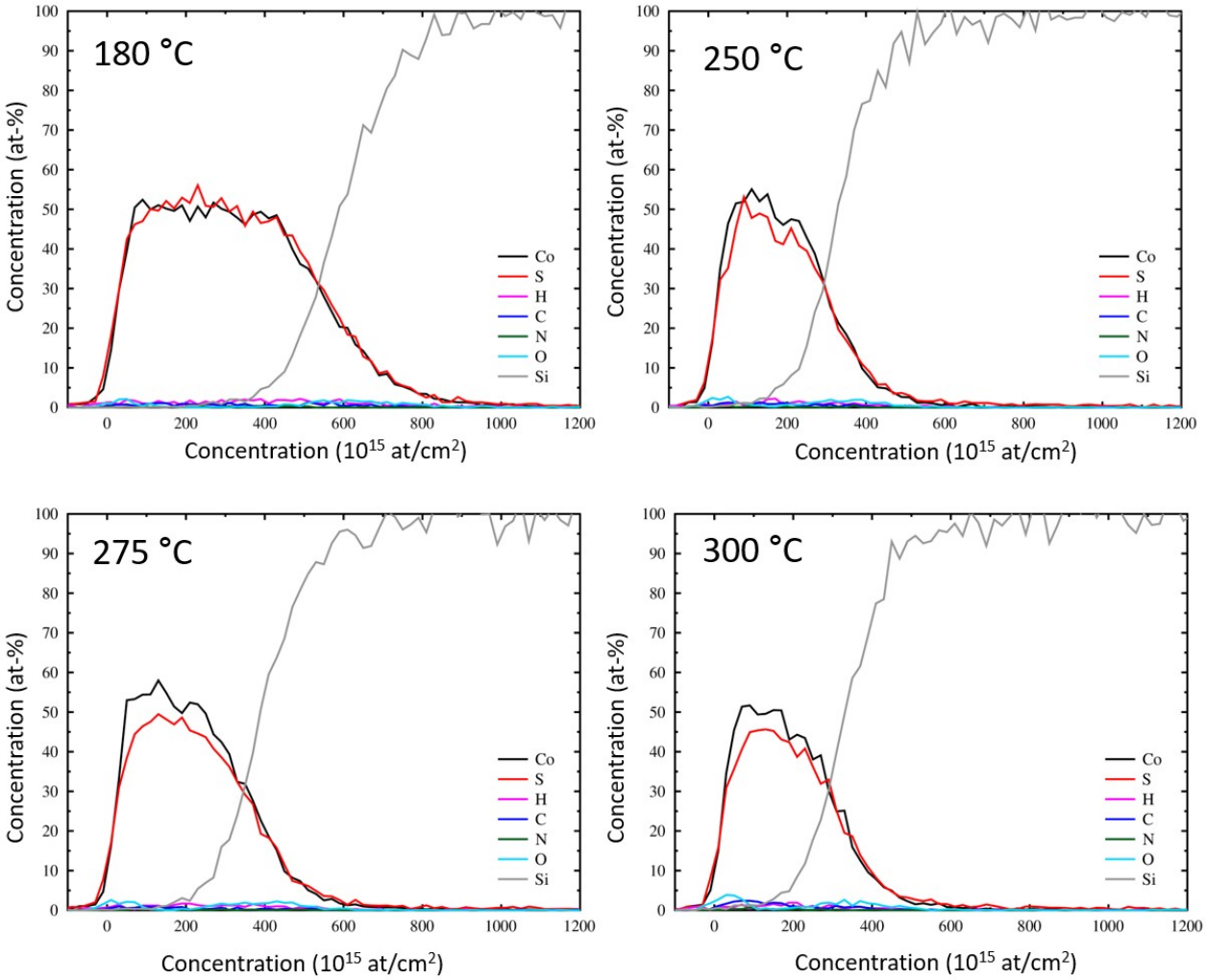

Fig. S11 ToF-ERDA elemental depth profiles of films deposited at different temperatures. The films were deposited on silicon (native oxide) using 1000 cycles except for the 180 °C film grown using 3000 cycles.

S6. Effect of film thickness

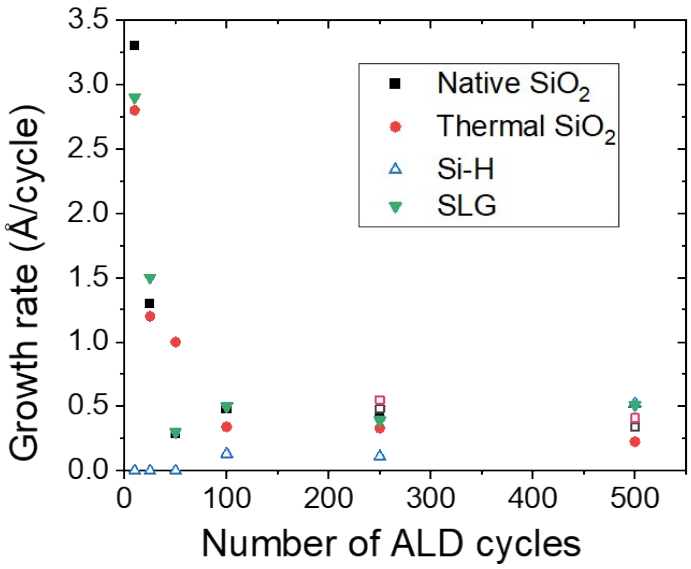

Fig. S12 Growth rate versus number of ALD cycles at 275 °C on different substrates. The data points were calculated using two adjacent points from Fig. 3a in the article (for example, 100 cycle data point represents thickness increase from 50 to 100 cycles divided by 50 cycles). Open and closed data points refer to thicknesses measured by EDS and XRR.

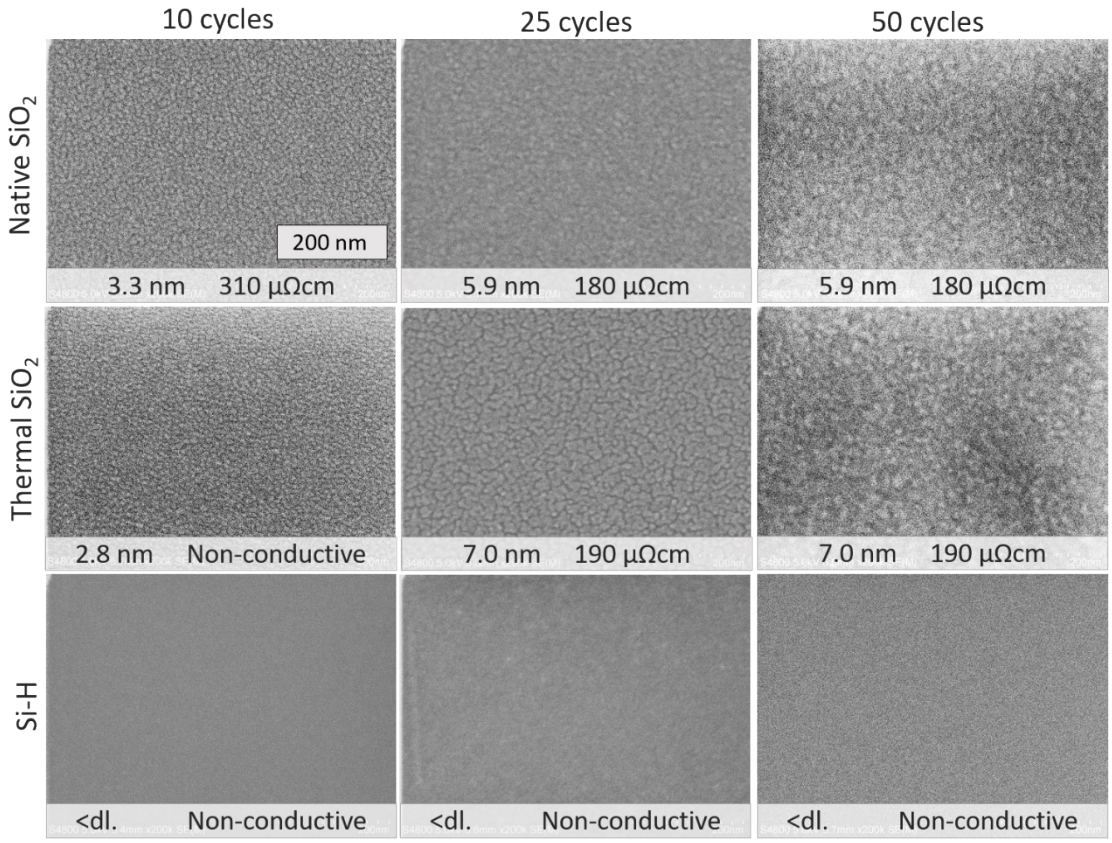

Fig. S13 SEM images, thicknesses, and resistivities of films deposited on different substrates at 275 °C using 10–50 ALD cycles. The thicknesses were measured by XRR.

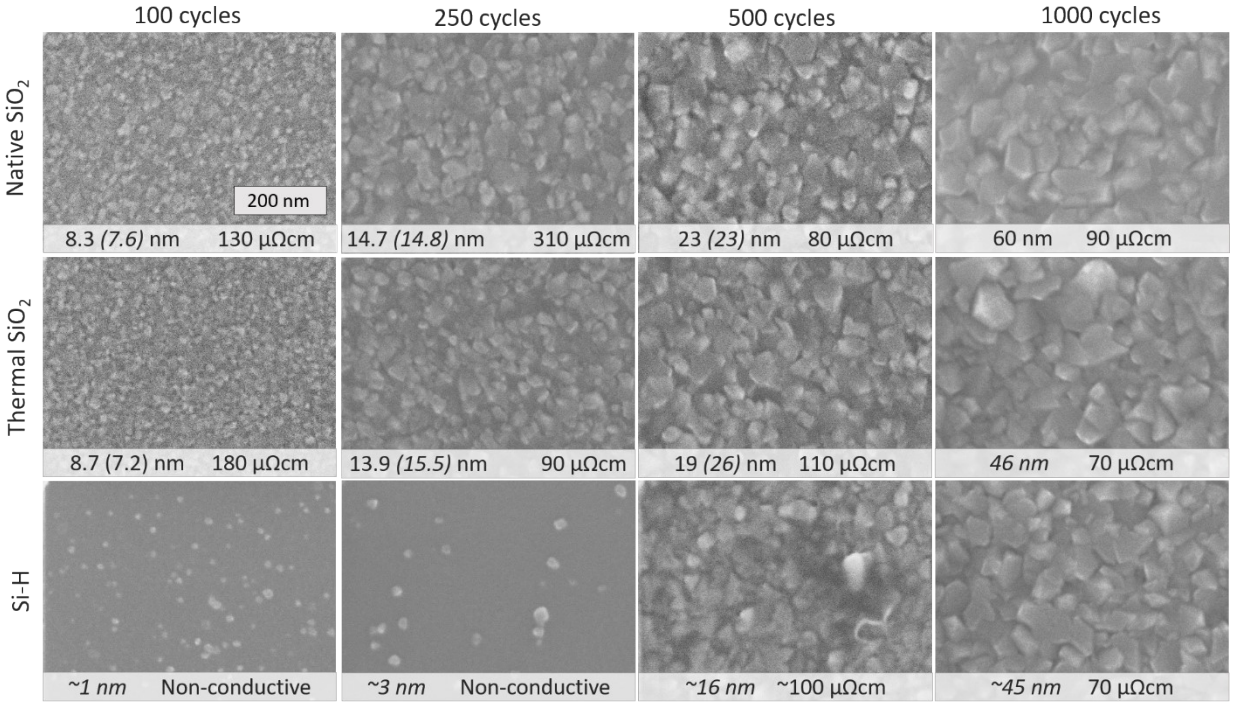

Fig. S14 SEM images, thicknesses, and resistivities of films deposited on different substrates at 275 °C using 100–1000 ALD cycles. The thicknesses in *italic* were measured by EDS, those in normal type by XRR. The values in parenthesis represent supporting measurements not used for resistivity calculations.

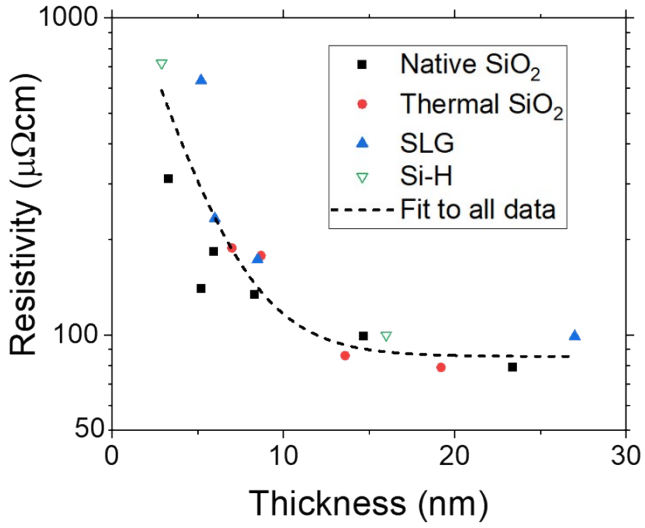

Fig. S15 Resistivity of films on different substrates versus thickness (calculated using data from Fig. 3a,b in the article). Open and closed data points refer to thicknesses measured by EDS and XRR.

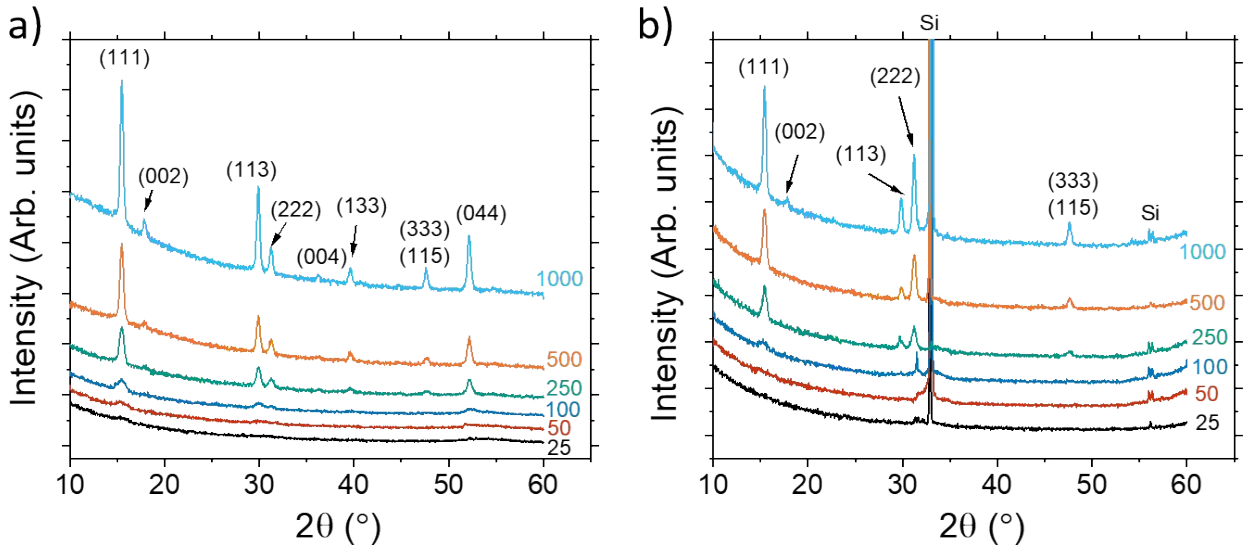

Fig. S16 (a) Grazing incidence and (b) θ-2θ X-ray diffractograms of films deposited using a varying number of ALD cycles. The films were deposited on silicon (native oxide) at 275 °C. All peaks were attributed to either Co_9S_8 (Miller indices marked) or Si substrate.

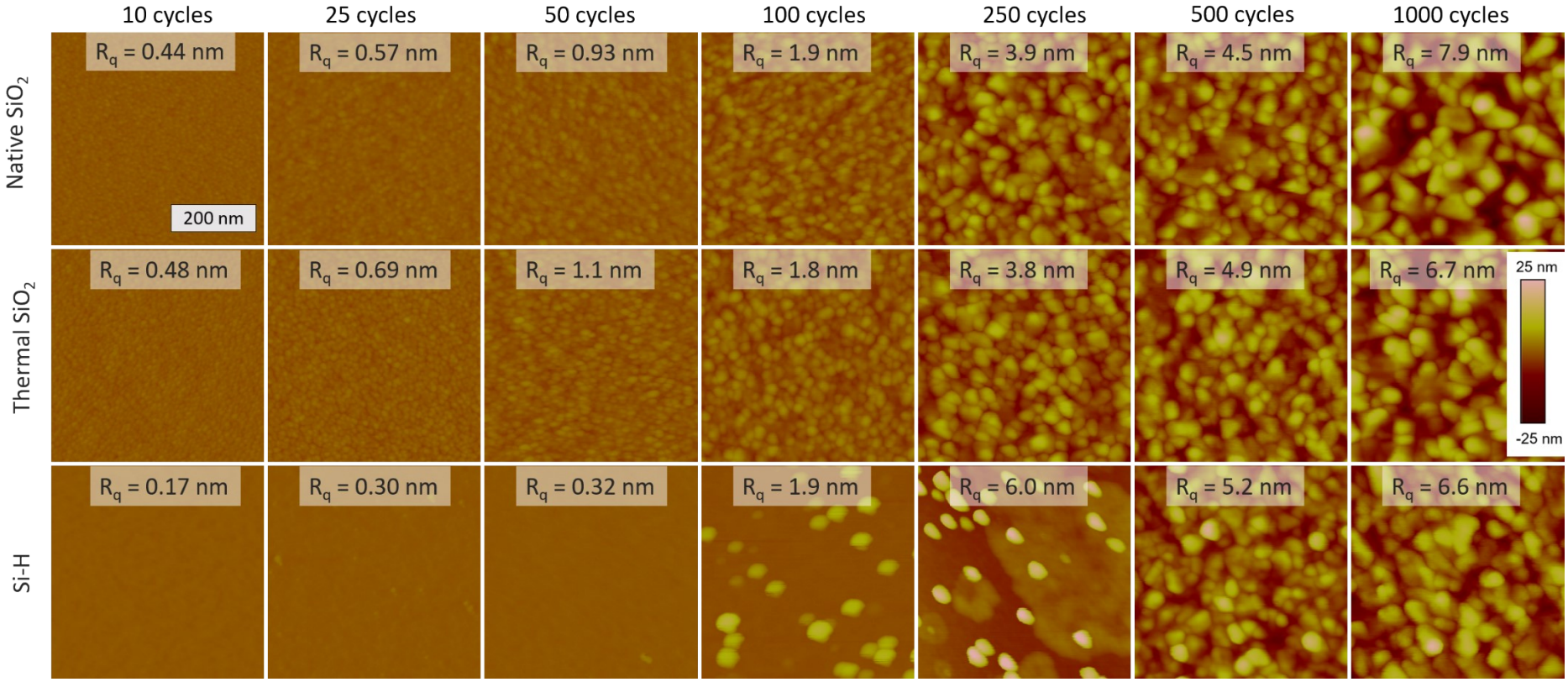

Fig. S17 Representative AFM images and root-mean-square roughness values (R_q, average of 3–5 images) of Co_9S_8 films deposited on native SiO_2, thermal SiO_2, and Si-H substrates with a varying number of cycles. All images are in the same lateral and height (color) scales.

S7. Deposition on different substrates

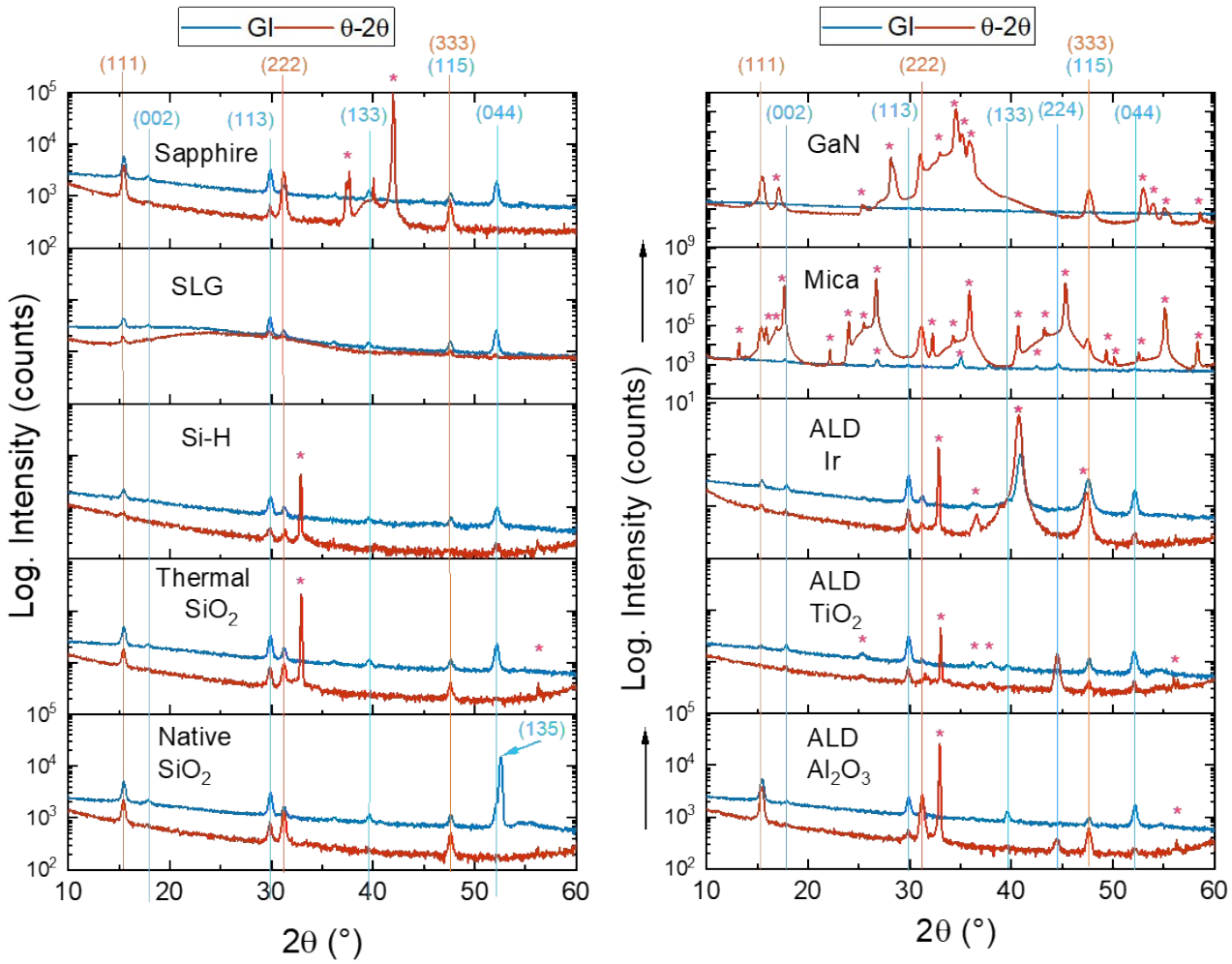

Fig. S18 Grazing incidence (blue) and θ-2θ (red) X-ray diffractograms of films deposited on different substrates at 275 °C using 1000 cycles. The Miller indices refer to Co_9S_8. The {111} reflections are marked with orange dashed lines and the reflections corresponding to other Co_9S_8 orientations with blue dashed lines. Asterisks mark substrate reflections. Note the different scale for the films deposited on mica and GaN.

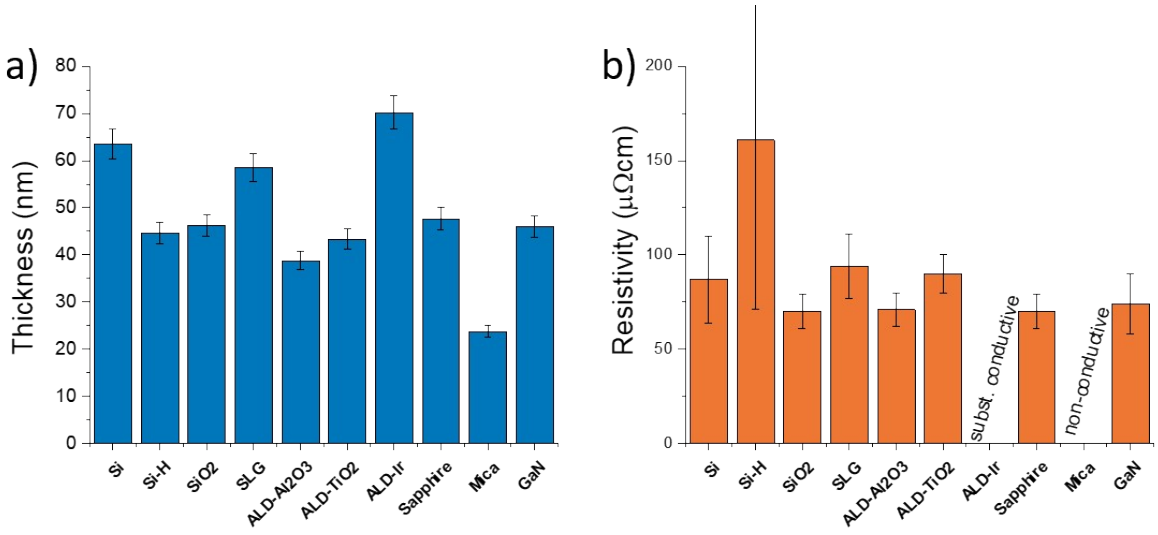

Fig. S19 (a) Thickness (EDS) and (b) resistivity of films deposited on different substrates at 275 °C using 1000 cycles. Error bars refer to estimated measurement uncertainty (5%) in a) and variation of resistance over the substrate (one standard deviation) in b). The high conductivity of ALD-Ir substrate prevented extraction of the Co_9S_8 resistivity. The resistivity of the film on mica was too high to be measured, which may be due to delamination of film from the flexible mica substrate.

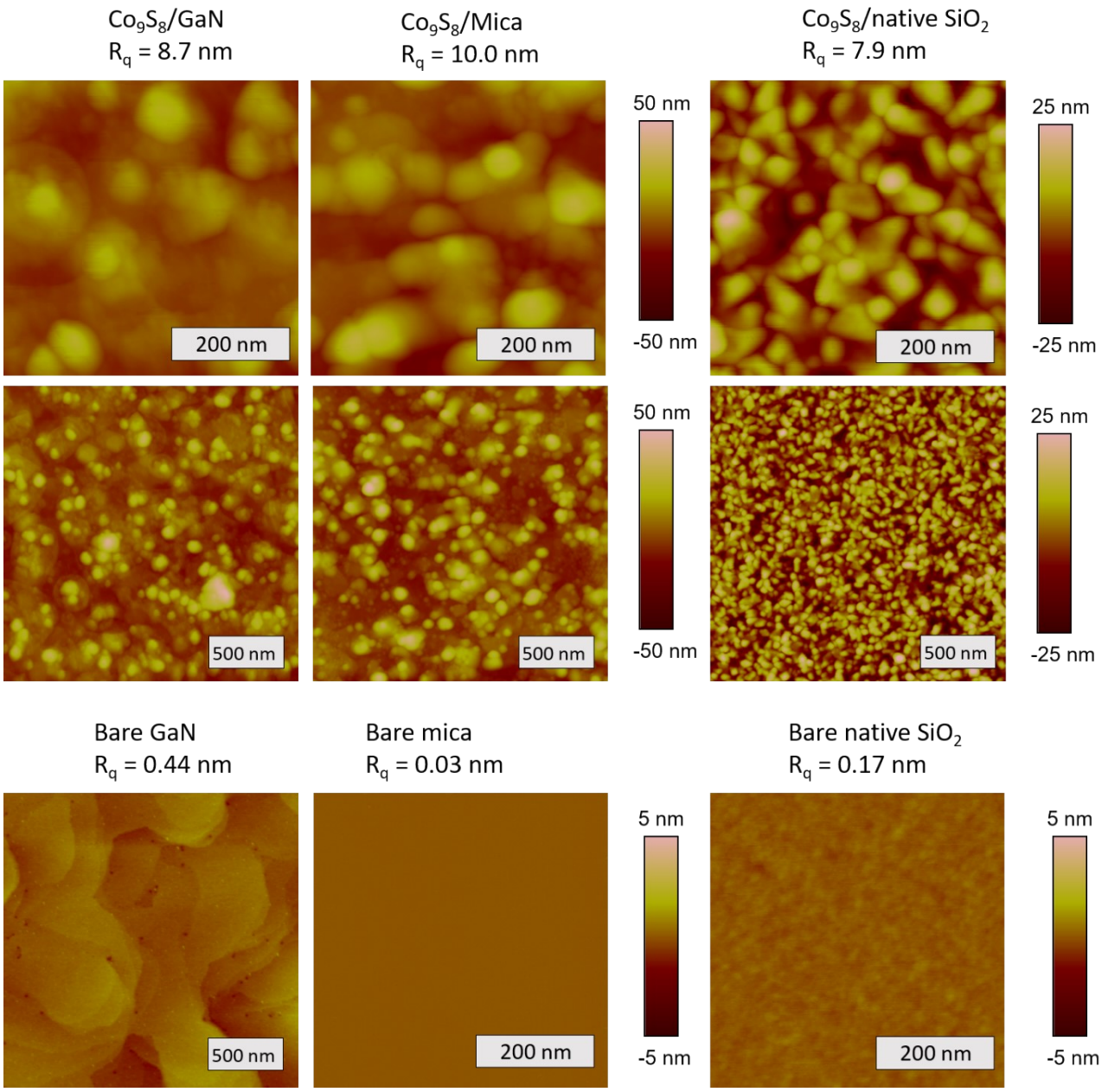

Fig. S20 AFM images and roughness (R_q) of Co_9S_8 films deposited on GaN, mica, and native SiO_2/Si substrates using 1000 cycles. Bare substrates are shown at the bottom for comparison. Note the varying height and lateral scales.

S8. Additional characterization and discussion of films on GaN

Herein, additional discussion as well as results on the Co_9S_8/GaN epitaxial system are provided. First, it is noted that the GaN(0001) surface is polar, i.e. it may be either Ga or N polar (terminated), more accurately described as (0001) and $(000\bar{1})$, respectively.[3] Both Ga and N atoms are arranged in an identical hexagonal lattice, so the Ga and N atoms can be interchanged in Fig. 5 d,e in the article for a N polar surface. Due to the large unit cell of Co_9S_8, a few different surfaces can be formed in the determined alignment. As an example, a puckered nearly hexagonal Co-S surface pictured in Fig. 5e in the article shows remarkable similarity to the hexagonal GaN surface. A similar surface with either Co or S termination can be formed. There is some variation in S-S and Co-Co distances from 3.38 to 3.54 Å (average 3.50 Å), i.e. from 6 to 11% longer (average 10%) than the shortest Ga-Ga (N-N) distance on the GaN surface (3.19 Å). Such a mismatch is considered too large for conventional epitaxial growth.[4]

Instead, special cases of epitaxy including van der Waals (vdW) epitaxy and domain matching epitaxy (DME) may be considered. In vdW epitaxy, no strong covalent bonds are formed between the film and the substrate.[5,6] In a typical case, vdW epitaxy is observed between layered 2D materials, whereas both GaN and Co_9S_8 have 3D crystal structures. Nevertheless, GaN is a known vdW epitaxy substrate.[7,8] In addition, there are some reports in the literature claiming growth of non-layered materials by vdW epitaxy, such as AlN on graphene,[9] M on MoS_2 (M = Ag, Au, Al, Cu, Pd, Pt),[10] ZnTe on graphene,[11] and ZnO on mica.[12] Reports of 3D-on-3D systems by van der Waals epitaxy are, however, scarce.

In domain matching epitaxy,[4] integral multiples of film and substrate lattice constants – or more generally lattice planes – match at the film-substrate interface. For example, 10% average lattice mismatch could be accommodated by matching 9 lattice planes of Co_9S_8 with 10 planes of GaN. Such matching of multiples of lattice constants, also known as coincident lattice matching, is also often

included in the description of vdW epitaxy systems.[13,14] For vdW epitaxy, it is usually assumed that no strain is built into the film,[5,6] whereas for DME the strain is concentrated at the film-substrate interface, also resulting in essentially strain-free films.[4] Both in-plane and out-of-plane XRD measurements suggested our Co_9S_8 films to be practically strain-free in the bulk of the film, which dominantly contributes to the diffracted intensity. The rather low disorder in the Co_9S_8/GaN system suggests this system follow the DME mechanism, where the film-substrate bonding is stronger compared to the vdW epitaxy.

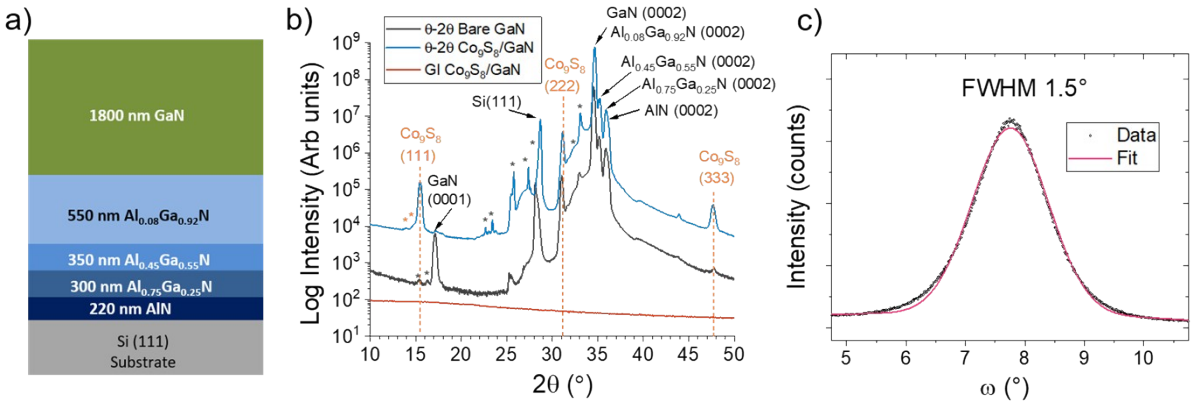

Fig. S21 (a) Schematic of the epitaxial GaN substrate on Si(111) with $Al_xGa_{1-x}N$ buffer layers. (b) X-ray diffractograms of Co_9S_8 film grown on GaN using 1000 cycles at 275 °C. Measurement of a bare substrate is shown for reference. Asterisks denote peaks originating from Cu Kβ and W Lα radiation from the non-monochromatic Cu X-ray tube with a W cathode (substrate in gray, Co_9S_8 in orange). The positions of the $Al_xGa_{1-x}N$ (0002) reflections agree with those determined from Vegard's law using lattice constants c = 5.186 Å for GaN and c = 4.981 Å for AlN. (c) ω scan of Co_9S_8 (111) reflection (15.5 °2θ).

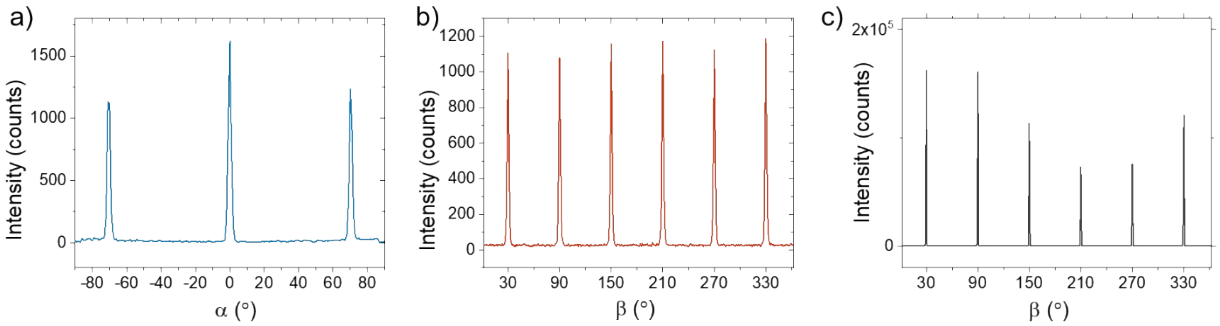

Fig. S22 Cuts extracted from in-plane pole figures shown in Fig. 5 in the article (Co_9S_8 on GaN). (a) α scan of $^{(111)}Co_9S_8$ reflection (90 °β, 15.5 °2θ). (b) β scan of $^{(111)}Co_9S_8$ reflection (20 °α, 15.5 °2θ). (c) β scan of $^{(\bar{1}102)}$GaN reflection (47 °α, 48.27 °2θ).

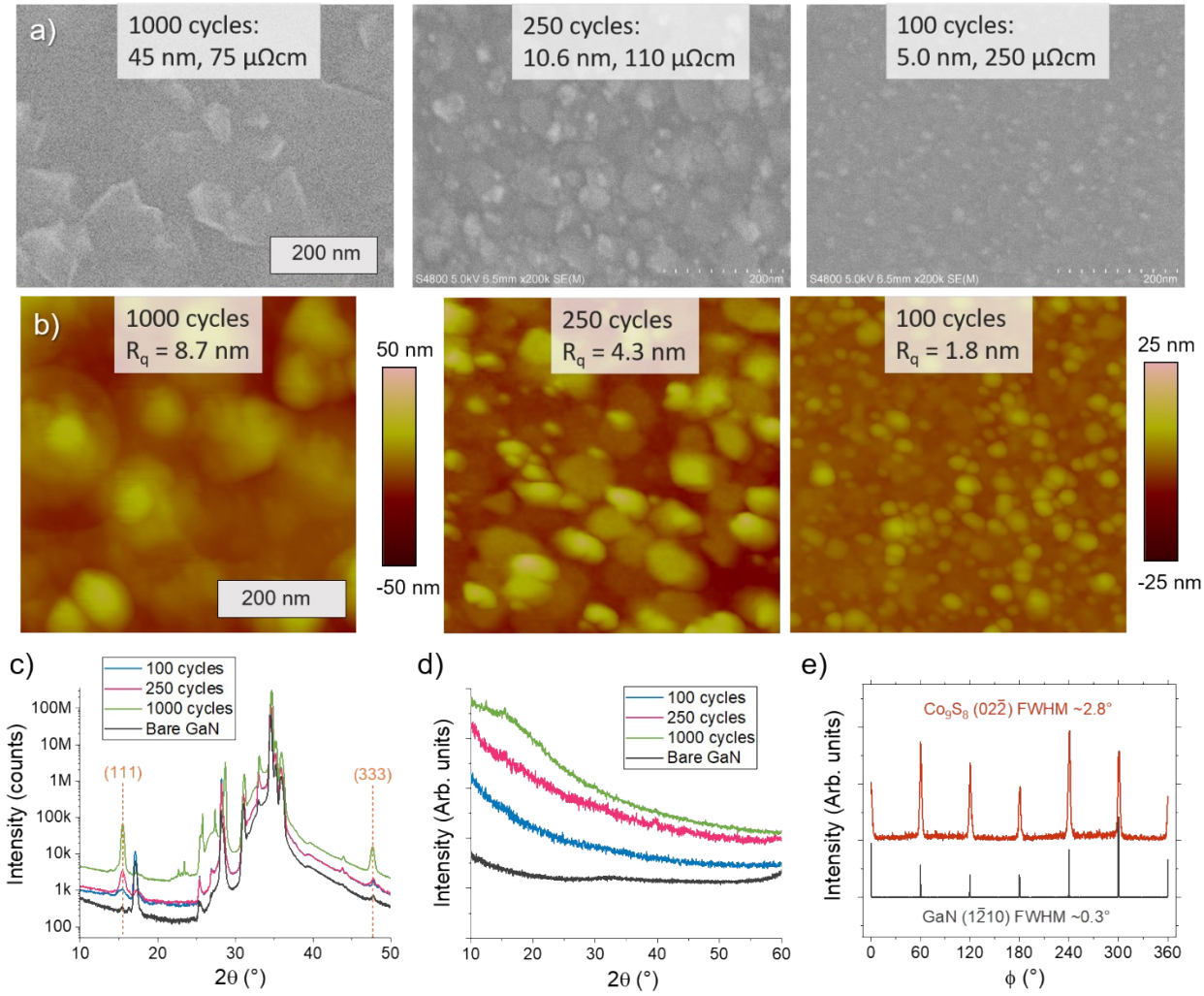

Fig. S23 Characterization of epitaxial Co_9S_8 films of different thicknesses on GaN. (a) SEM images with EDS thicknesses and resistivities and (b) AFM images with roughness shown, (c) θ-2θ and (d) grazing incidence X-ray diffractograms of Co_9S_8 films deposited on GaN using 100–1000 cycles. (e) In-plane φ scans of $^{(02\bar{2})}Co_9S_8$ (25.35 °2θχ) and $^{(1\bar{2}10)}$GaN (57.95 °2θχ) reflections of a 250 cycle Co_9S_8 film on GaN. The presence of only {111} reflections in (c), lack of reflections in (d), and presence of six sharp peaks in (e) confirms the epitaxial nature of the 250 cycle film with a similar degree of epitaxial quality to the 1000 cycle film. The data in (e) has been vertically offset for clarity.

S9. Additional characterization of films on mica

Co_9S_8 films deposited on mica exhibited even stronger (111) out-of-plane texture than the films on GaN, as shown by a rocking curve FWHM of 0.18° (Fig. S24). In contrast to GaN, an in-plane pole figure revealed six very broad peaks on top of a faint continuous ring at 19.5 °α (Fig. S25a,b). Detailed in-plane φ scan measurements of the $(04\bar{4})Co_9S_8$ reflection suggested that the six broad peaks were composed of at least three peaks each, the most intense peak in the middle (rotated by 30° with respect to the (020)mica reflection) with weaker peaks rotated by ±15° (Fig. S25c). In addition to a larger amount of domains, much larger in-plane disorder compared to the Co_9S_8/GaN system was observed, as shown by the relatively large FWHM of the in-plane $(04\bar{4})Co_9S_8$ peaks (on average 9.6° and 14.3° for the orientations denoted 0 and ±15°) as well as detection of $(2\bar{2}0)Co_9S_8$ reflection at all angles of sample rotation (φ, Fig. S25d).

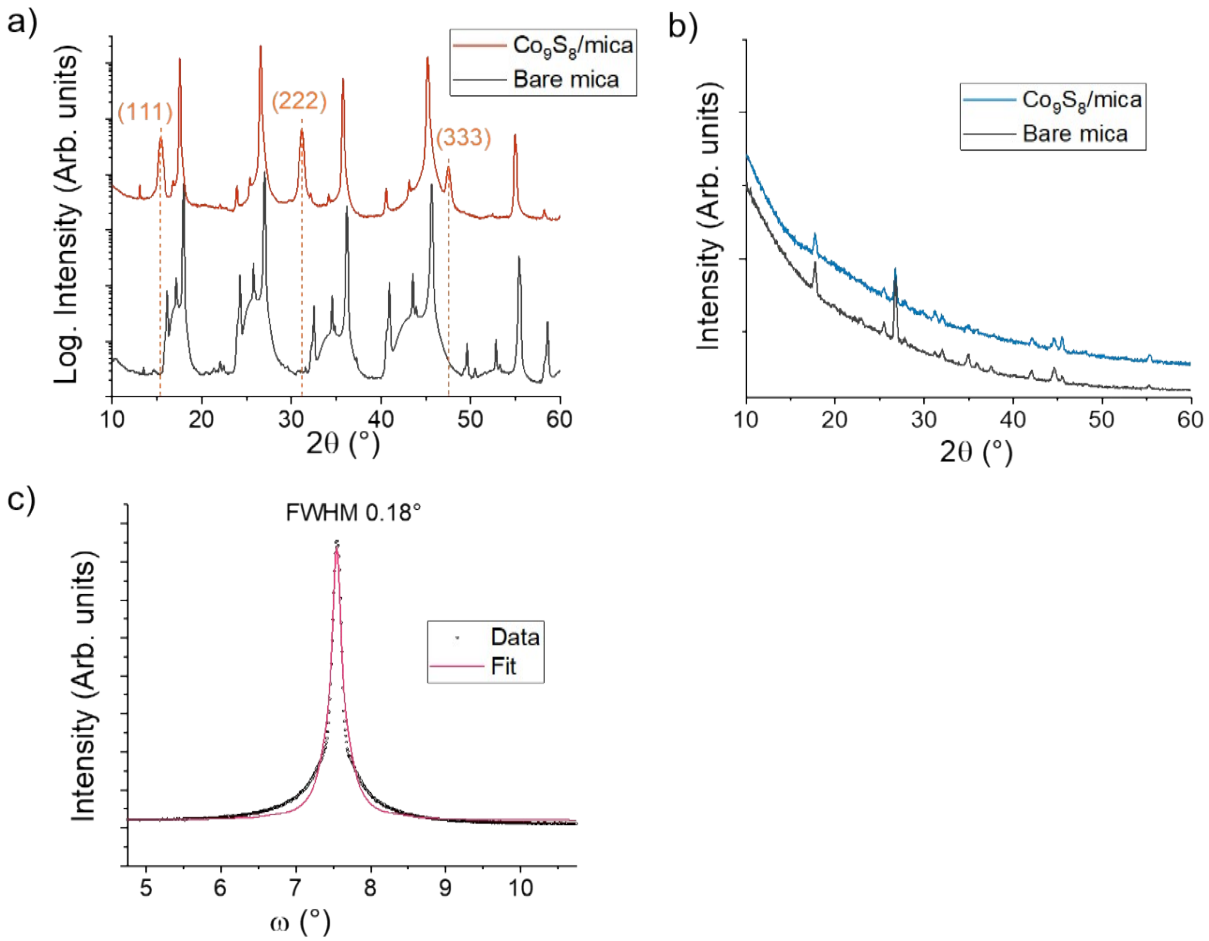

Fig. S24 (a) θ-2θ and (b) grazing incidence X-ray diffractograms of Co_9S_8 film deposited on mica (1000 cycles at 275 °C) as well as those of the bare substrate. (c) Rocking curve of the $^{(111)}Co_9S_8$ reflection. The occurrence of only $\{111\}$ reflections in (a), lack of film reflections in (b) (only weak substrate peaks from the substrate are observed) and very sharp peak in (c) indicates strong (111) texture of Co_9S_8.

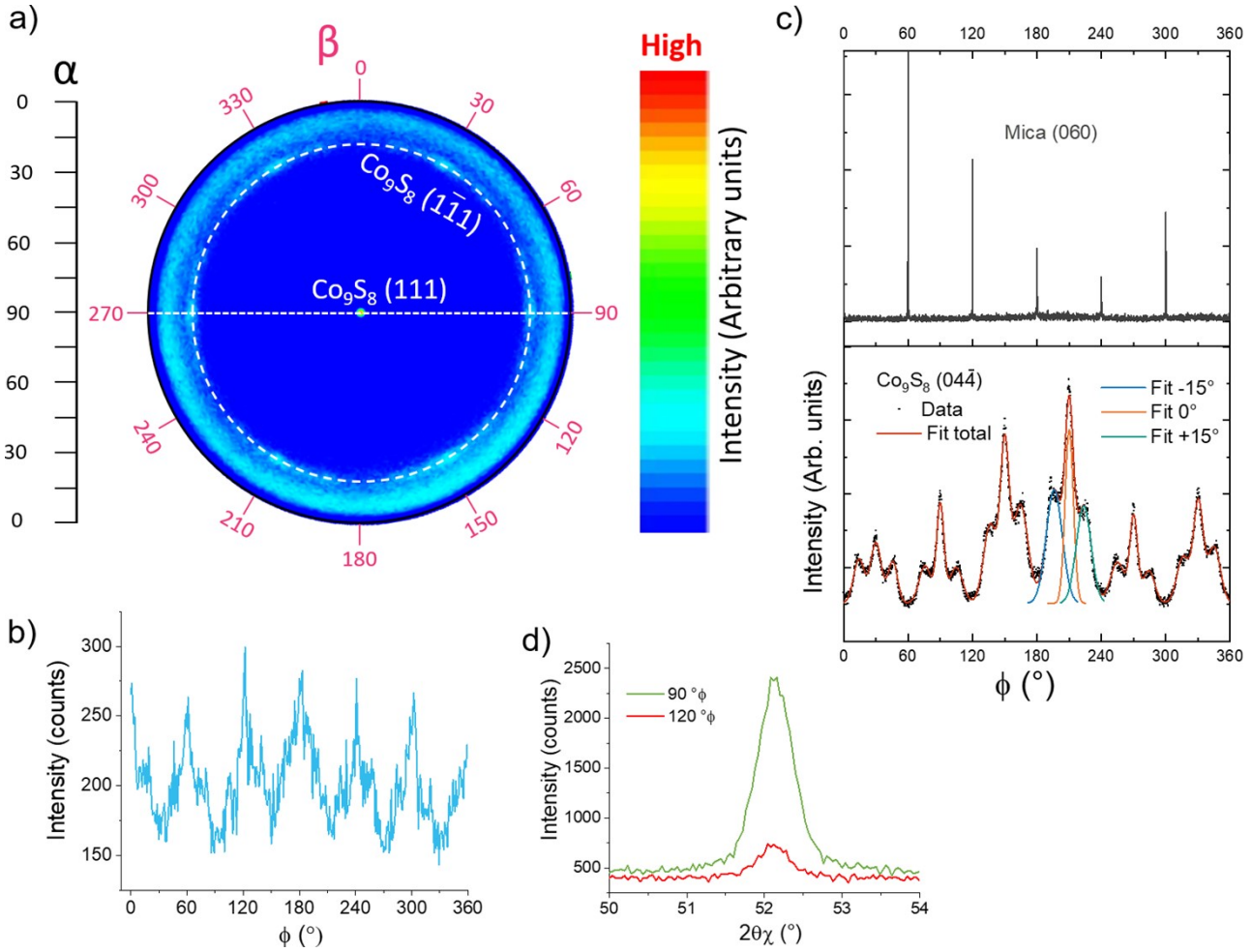

Fig. S25 (a) In-plane pole figure at 15.5 °2θ showing the out-of-plane $^{(111)}Co_9S_8$ reflection in the middle (90 °α) and $^{(\bar{1}11)}$ reflections tilted by 70.5° (19.5 °α). The broad circle around 10 °α is a part of the background. (b) β scan extracted from the pole figure (20 °α, 15.5 °2θ). (c) In-plane φ scans of $^{(04\bar{4})}Co_9S_8$ (52.1 °2θχ) and $^{(060)}$mica (61.84 °2θχ) reflections. Three fitted peaks representing differently oriented Co_9S_8 domains are shown. The data has been vertically offset for clarity. (d) In-plane 2θχ scans around the $^{(04\bar{4})}Co_9S_8$ reflection (52.1 °2θχ) at two phi angles, one (90 °φ) corresponding to preferred Co_9S_8 in-plane orientation in (c), one (120 °φ) to orientation with a minimum in intensity. The observation of peak at 120 °φ, albeit much weaker than at 90 °φ, suggests presence of misaligned polycrystalline domains.

S10. Additional characterization of films on sapphire

On the third single-crystalline surface evaluated, c-plane sapphire or α-Al_2O_3(0001), the Co_9S_8 displayed much weaker (111) texture, although it was still stronger compared to silicon (Fig. S26). An out-of-plane registration is a necessary (yet not sufficient) condition for epitaxy. In absence of it, no detailed studies on the in-plane alignment were conducted.

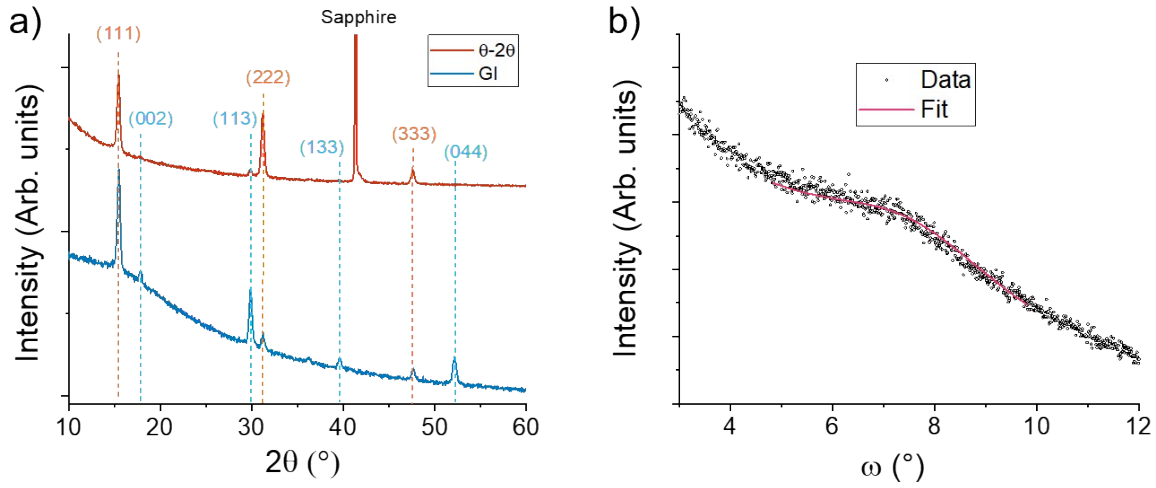

Fig. S26 (a) X-ray diffractograms of Co_9S_8 film deposited on sapphire (1000 cycles at 275 °C) and (b) a rocking curve of the $^{(111)}Co_9S_8$ reflection. The observation of peaks in the grazing incidence diffractograms and the weak intensity and broadness of the peak in (b) suggest much weaker $^{(111)}$ texture compared to Co_9S_8 films on the other single crystalline surfaces, GaN and mica.

S11. Additional HTXRD measurements

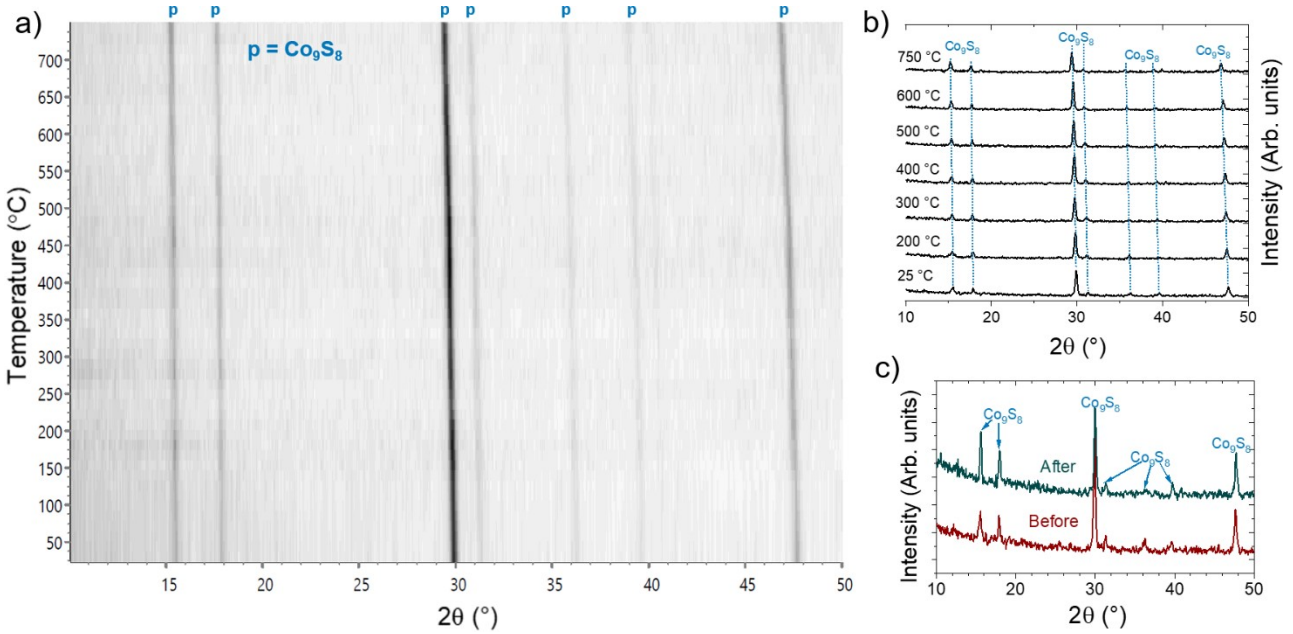

Fig. S27 (a) High-temperature grazing incidence X-ray diffractograms during heating in a N_2 atmosphere (30 mbar) from 25 to 750 °C (measured at 25 °C intervals), where light and dark represent low and high intensities, respectively. (b) Selected diffractograms measured at different temperatures and (c) diffractograms measured at 25 °C before and after heating to 750 °C. The studied film was deposited on silicon (native oxide) at 275 °C using 1000 cycles.

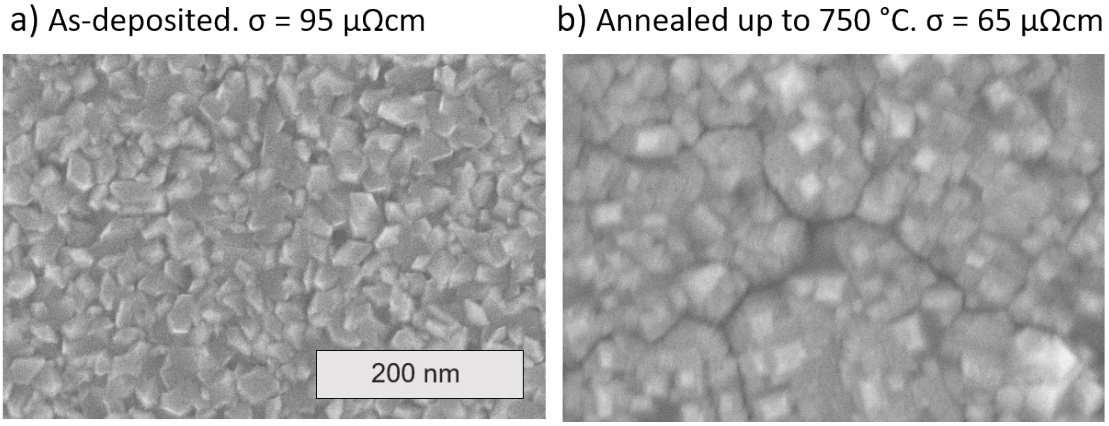

Fig. S28 SEM images and resistivities of Co_9S_8 films (a) as-deposited (1000 cycles, 275 °C, on silicon with native oxide) and (b) after a HTXRD measurement in a N_2 atmosphere (30 mbar) up to 750 °C.

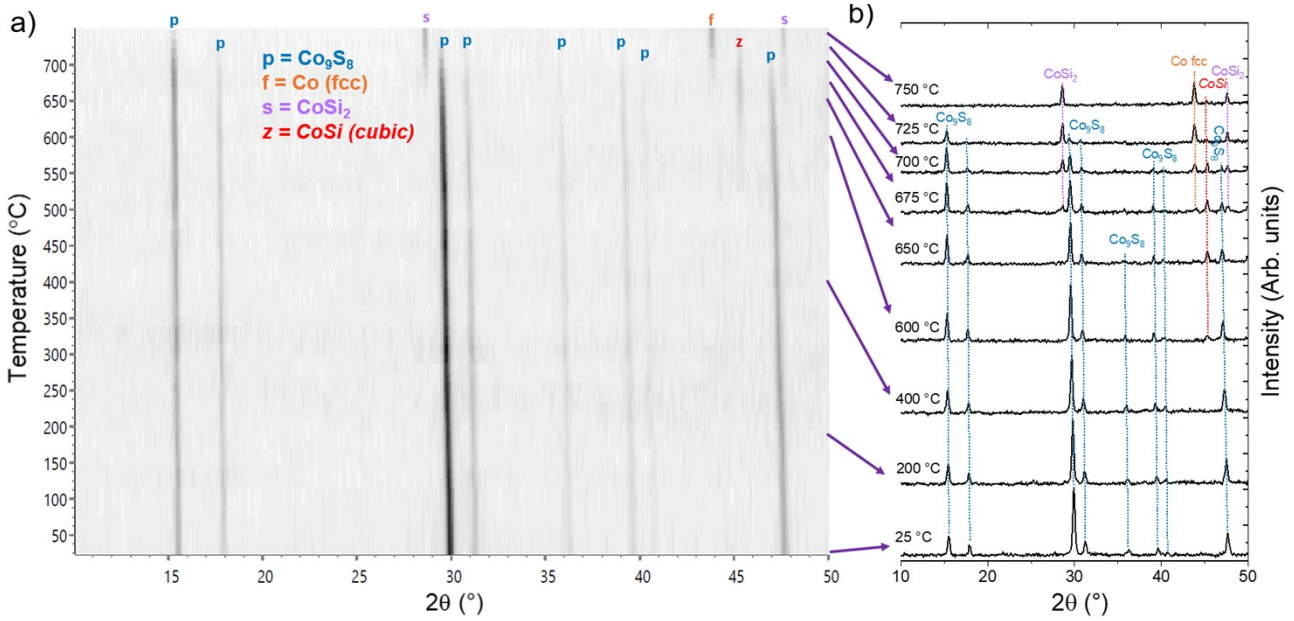

Fig. S29 (a) High-temperature grazing incidence X-ray diffractograms during heating in dynamic vacuum (approximately 10^{-5} mbar) from 25 to 725 °C (measured at 25 °C intervals), where light and dark represent low and high intensities, respectively. (b) Selected diffractograms measured at different temperatures. The studied film was deposited on silicon (native oxide) at 275 °C using 1000 cycles.

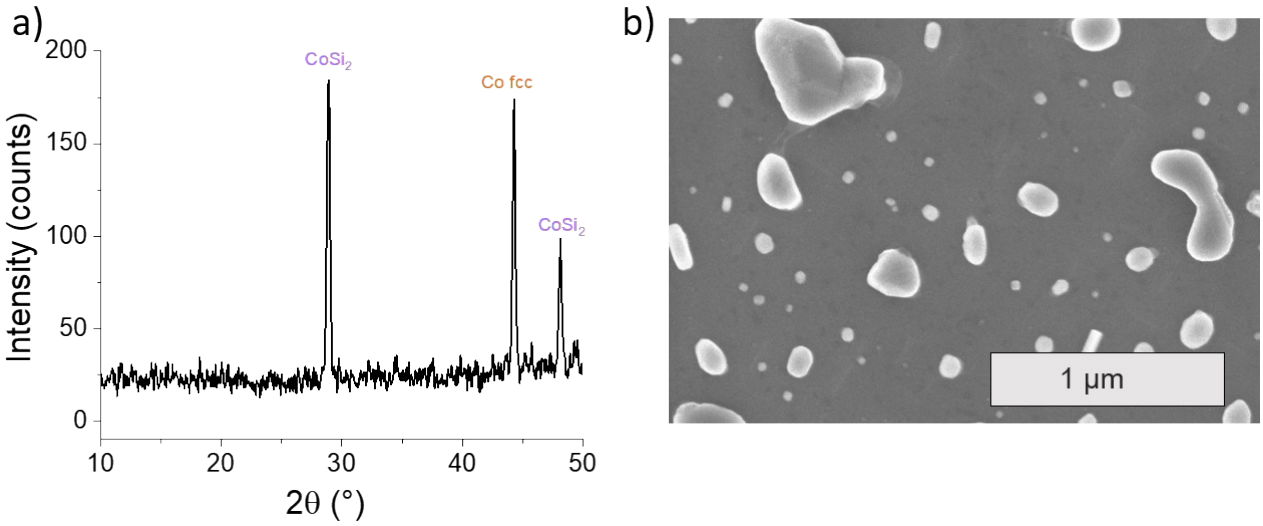

Fig. S30 (a) Grazing incidence X-ray diffractogram (at 25 °C) and (b) SEM image after a HTXRD measurement in vacuum (approximately 10^{-5} mbar) up to 725 °C. The film was deposited on silicon (native oxide) at 275 °C using 1000 cycles.

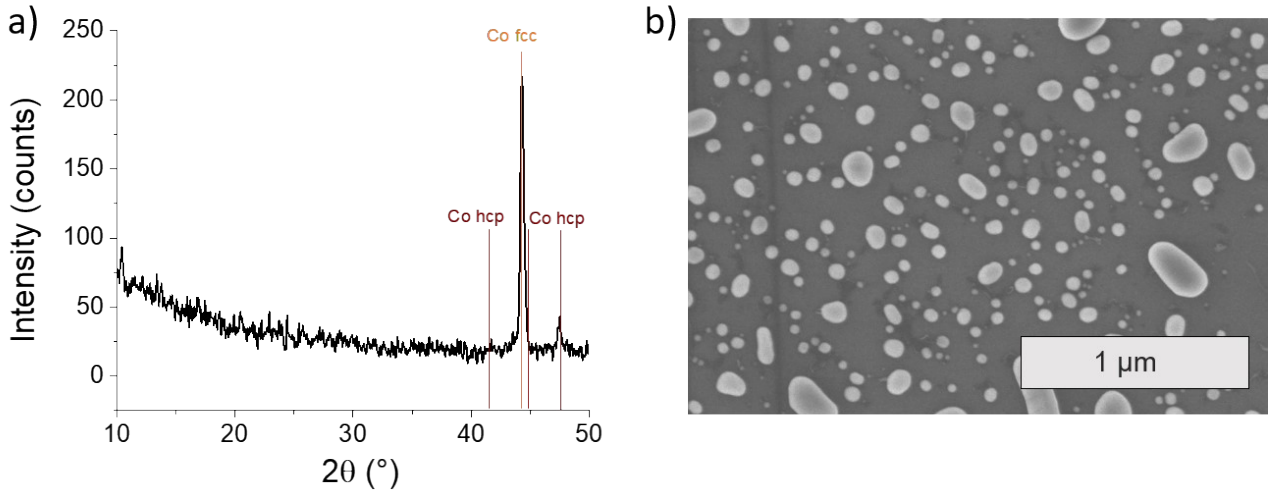

Fig. S31 (a) Grazing incidence X-ray diffractogram (at 25 °C) and (b) SEM image after a HTXRD measurement in a forming gas atmosphere (10% H_2 / 90% N_2, 1 atm) up to 725 °C. The film was deposited on silicon (native oxide) at 275 °C using 1000 cycles.

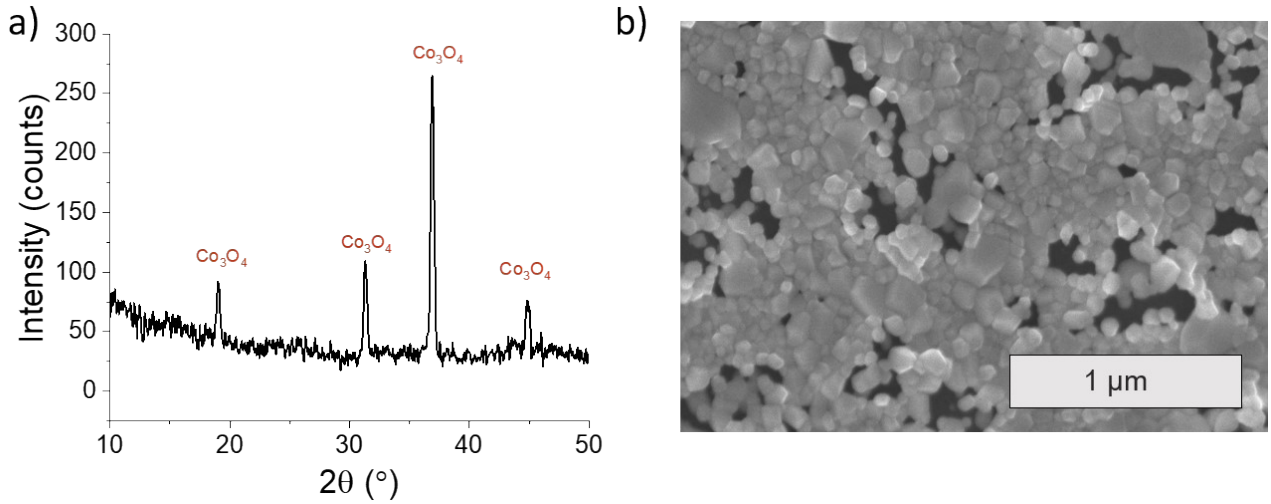

Fig. S32 (a) Grazing incidence X-ray diffractogram (at 25 °C) and (b) SEM image after a HTXRD measurement in air up to 725 °C. The film was deposited on silicon (native oxide) at 275 °C using 1000 cycles.

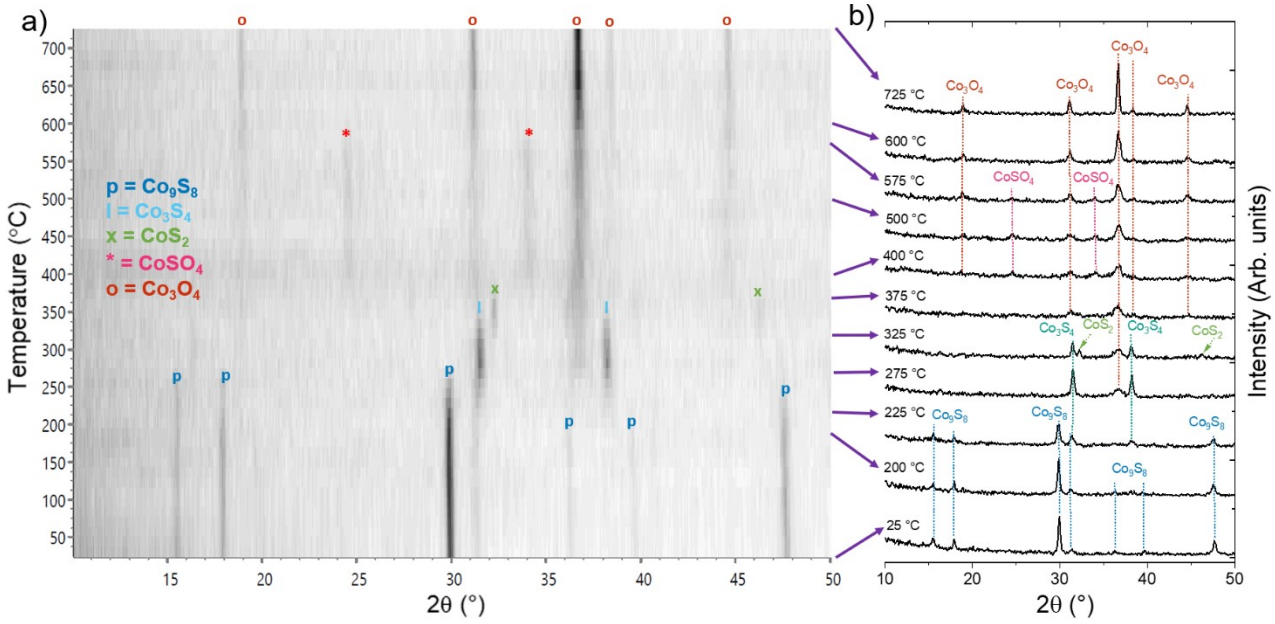

Fig. S33 (a) High-temperature grazing incidence X-ray diffractograms during heating in a O_2 atmosphere (1 atm) from 25 to 725 °C (measured at 25 °C intervals), where light and dark represent low and high intensities, respectively. (b) Selected diffractograms measured at different temperatures. The studied film was deposited on silicon (native oxide) at 275 °C using 1000 cycles.

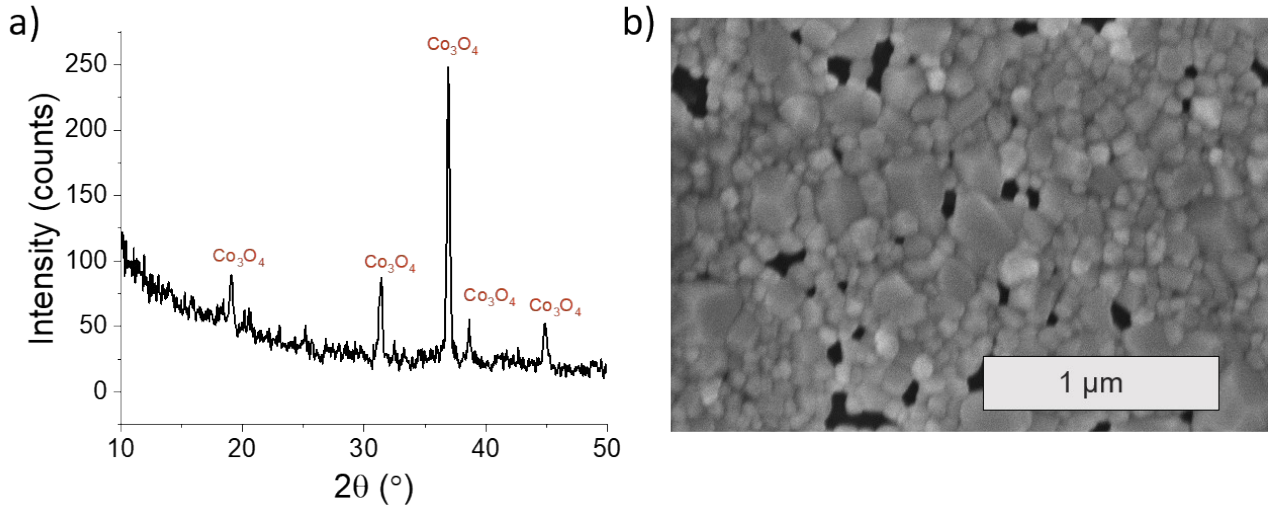

Fig. S34 (a) Grazing incidence X-ray diffractogram (at 25 °C) and (b) SEM image after a HTXRD measurement in an O_2 atmosphere (1 atm) up to 725 °C. The film was deposited on silicon (native oxide) at 275 °C using 1000 cycles.

S12. References

1 R. L. Puurunen, Correlation between the growth-per-cycle and the surface hydroxyl group concentration in the atomic layer deposition of aluminum oxide from trimethylaluminum and water, *Appl. Surf. Sci.*, 2005, **245**, 6.

2 O. Nilsen, O. B. Karlsen, A. Kjekshus and H. Fjellvåg, Simulation of growth dynamics in atomic layer deposition. Part II. Polycrystalline films from cubic crystallites, *Thin Solid Films*, 2007, **515**, 4538.

3 V. M. Bermudez, The fundamental surface science of wurtzite gallium nitride, *Surf. Sci. Rep.*, 2017, **72**, 147.

4 J. Narayan and B. C. Larson, Domain epitaxy: A unified paradigm for thin film growth, *J. Appl. Phys.*, 2003, **93**, 278.

5 A. Koma, Van der Waals epitaxy - a new epitaxial growth method for a highly lattice-mismatched system, *Thin Solid Films*, 1992, **216**, 72.

6 L. A. Walsh and C. L. Hinkle, van der Waals epitaxy: 2D materials and topological insulators, *Appl. Mater. Today*, 2017, **9**, 504.

7 Z. Chen, H. Liu, X. Chen, G. Chu, S. Chu and H. Zhang, Wafer-Size and Single-Crystal $MoSe_2$ Atomically Thin Films Grown on GaN Substrate for Light Emission and Harvesting, *ACS Appl. Mater. Interfaces*, 2016, **8**, 20267.

8 C. Liu, H. Huang, W. Choi, J. Kim, K. Jung, W. Sun, N. Tansu, W. Zhou, H. Kuo and X. Li, Hybrid Integration of n-MoS_2 /p-GaN Diodes by Quasi-van der Waals Epitaxy, *ACS Appl. Electron. Mater.*, 2020, **2**, 419.

9 Y. Xu, B. Cao, Z. Li, D. Cai, Y. Zhang, G. Ren, J. Wang, L. Shi, C. Wang and K. Xu, Growth Model of van der Waals Epitaxy of Films: A Case of AlN Films on Multilayer Graphene/SiC, *ACS Appl. Mater. Interfaces*, 2017, **9**, 44001.

10 A. C. Domask, K. A. Cooley, B. Kabius, M. Abraham and S. E. Mohney, Room Temperature van der Waals Epitaxy of Metal Thin Films on Molybdenum Disulfide, *Cryst. Growth Des.*, 2018, **18**, 3494.

11 X. Sun, Z. Chen, Y. Wang, Z. Lu, J. Shi, M. Washington and T.-M. Lu, van der Waals epitaxial ZnTe thin film on single-crystalline graphene, *J. Appl. Phys.*, 2018, **123**, 025303.

12 S. Ke, J. Xie, C. Chen, P. Lin, X. Zeng, L. Shu, L. Fei, Y. Wang, M. Ye and D. Wang, Van der Waals epitaxy of Al-doped ZnO film on mica as a flexible transparent heater with ultrafast thermal response, *Appl. Phys. Lett.*, 2018, **112**, 031905.

13 J. E. Boschker, L. A. Galves, T. Flissikowski, J. M. J. Lopes, H. Riechert and R. Calarco, Coincident-site lattice matching during van der Waals epitaxy, *Sci. Rep.*, 2016, **5**, 18079.

14 D. S. Koda, F. Bechstedt, M. Marques and L. K. Teles, Coincidence Lattices of 2D Crystals: Heterostructure Predictions and Applications, *J. Phys. Chem. C*, 2016, **120**, 10895.